

# Molecular Dynamics Simulations of a Pressure-induced Glass Transition

Shelly L. Shumway, Andrew S. Clarke\* and Hannes Jónsson

*Department of Chemistry, BG-10, University of Washington, Seattle, Washington 98195*

## Abstract

We simulate the compression of a two-component Lennard-Jones liquid at a variety of constant temperatures using a molecular dynamics algorithm in an isobaric-isothermal ensemble. The viscosity of the liquid increases with pressure, undergoing a broadened transition into a structurally arrested, amorphous state. This transition, like the more familiar one induced by cooling, is correlated with a significant increase in icosahedral ordering. In fact, the structure of the final state, as measured by an analysis of the bonding, is essentially the same in the glassy, frozen state whether produced by squeezing or by cooling under pressure. We have computed an effective hard-sphere packing fraction at the transition, defining the transition pressure or temperature by a cutoff in the diffusion constant, analogous to the traditional laboratory definition of the glass transition by an arbitrary, low cutoff in viscosity. The packing fraction at this transition point is not constant, but is consistently higher for runs compressed at higher temperature. We show that this is because the transition point defined by a constant cutoff in the diffusion constant is not the same as the point of structural arrest, at which further changes in pressure induce no further structural changes, but that the two alternate descriptions may be reconciled by using a thermally activated cutoff for the diffusion constant. This enables estimation of the characteristic activation energy for diffusion at the point of structural arrest.

## 1. Introduction

The glass transition most often studied is that which occurs when a viscous liquid forms a glass upon reduction of the temperature at constant, usually zero, pressure. A transition into a solid amorphous structure could alternately be obtained at constant temperature by applying pressure. We examine this latter transition here, through molecular dynamics [MD] simulations of a two-component Lennard-Jones [LJ] system.

The combination of pressure and temperature effects results in behavior not seen in cooling studies without pressure. We are particularly interested in the relationship between structural and dynamical properties, and we address a non-trivial aspect of this relationship in this paper, demonstrating that diffusion, a dynamical property, is correlated in an activated, non-linear way with the structural changes that occur as the material is compressed.

## 2. Method of Simulation

We, like many others who have studied glassy behavior through computer simulations,<sup>1,2</sup> have used a two-component Lennard-Jones [LJ] system as the model: interactions between atoms are described by the pair potential  $v_{\alpha\beta} = 4\epsilon[(\sigma_{\alpha\beta}/r)^{12} - (\sigma_{\alpha\beta}/r)^6]$ . All data reported here were obtained for a 2000-atom system consisting of 1600 small atoms with  $\sigma_{11} = 1$  and 400 larger atoms with  $\sigma_{22} = 1.2$ , with  $\sigma_{12} = 1.1$  for the interaction between the two different types. The other parameters, mass  $m$  and energy  $\epsilon$ , were the same for all atoms. We used periodic boundary conditions in all three directions. The time step for integration was  $0.01\tau$ , where  $\tau = (m\sigma_{11}^2/\epsilon)^{(1/2)}$ .

We have simulated with a molecular dynamics algorithm in an isobaric-isothermal ensemble, using Andersen's constant pressure method<sup>3</sup> combined with stochastic collisions. A detailed description of this algorithm is given in the appendices to a paper by Fox and Andersen.<sup>4</sup> Andersen's method adds an extra degree of freedom, the total volume, to the Lagrangian for the system. The volume adjusts freely to maintain a nearly constant, though

fluctuating, pressure. We show in Appendix A how to calculate a reasonable value for the “piston mass,” which determines the coupling strength of the volume term. The stochastic collisions involve effectively colliding a few randomly selected particles each time step with a heat bath that has a Boltzmann distribution of velocities at the correct temperature. Andersen has demonstrated<sup>3</sup> that the combination of his constant pressure method with such stochastic collisions in standard molecular dynamics results in a correct isothermal-isobaric ensemble: the time-averaged value  $\langle F \rangle$  for any quantity  $F$  converges to the correct isobaric-isothermal ensemble average  $F_{NPT}$  in the limits of  $t \rightarrow \infty$  and  $N \rightarrow \infty$ .

We have run at five different constant temperatures, in each case with pressure increasing over time as shown in Figure 1. At a temperature of  $T^* = kT/\epsilon = 0.8$ , we have examined the behavior at several intermediate pressures more closely by running for a long time at constant pressure with initial configurations given by the endpoints of the plateaus in the rapidly-increasing-pressure runs, as shown in the inset to Figure 1. Pressure is given throughout this paper in units of  $\epsilon/\sigma_{11}^3$ , which would be about 425 bars if the smaller particles were argon.

### 3. Diffusion

The self-diffusion constant  $D_\alpha = (d/dt \langle x_\alpha^2 \rangle)/6$  is a convenient measure of how freely atoms of type  $\alpha$  are able to move around within the system. As the liquid becomes more viscous and relaxations freeze out, atoms become stuck in their places and the diffusion constant falls. This is seen in Figure 2 for an average diffusion constant<sup>5</sup>  $D = (D_1 + D_2)/2$  for each of the constant temperatures we simulated. At a temperature of  $T^* = 0.6$ , the diffusion constant falls to nearly zero by the rather low pressure of 6, while at a higher temperature of  $T^* = 1.5$ , diffusion persists to much higher pressures. We have fit the data for the three lower temperatures to an exponential function  $D = Ae^{-BP}$ , for  $T^* = 1.0$  to a sum of two exponentials,  $D = Ae^{-BP} + Ce^{-EP}$ , and for  $T^* = 1.5$  to a sum of three exponentials. Our least-squares fitting program returned  $\chi^2 < 4 \times 10^{-5}$  in each case. The

single exponential was not used for the two highest temperatures because the fit was bad, with  $\chi^2$  two orders of magnitude higher for  $T^* = 1.0$  and four for  $T^* = 1.5$ .

Experimentally, the glass transition in a real material is defined by an arbitrary cutoff in viscosity ( $\eta$ ): by  $\eta \sim 10^{14}$  poise, the liquid is acting solid on human time scales. Since the behavior of the diffusion coefficient  $D$  is similar<sup>6,7</sup> to that of  $1/\eta$  in glassy materials, the transition could alternately be defined in terms of an arbitrary cutoff in  $D$ ;  $\eta$  is easier to measure experimentally,  $D$  is easier in computer simulations. We define our glass transition pressure  $P_g$ , which is plotted in Figure 3, as the point at which  $D$  falls below 0.001, in units of  $\sigma_{11}^2/\tau$ , using the fitting functions described above to determine this point. Some other cutoff could equally well have been chosen; the behavior of the  $P_g$  versus  $T$  curve is qualitatively the same for cutoffs ranging from 0.0005 to 0.004, as shown in the inset to Figure 3. Of course, any diffusion measured in our simulations corresponds to a much lower viscosity than  $10^{14}$  poise. Our cutoff of  $D = 0.001$  corresponds to about  $5 \times 10^{-7}$  cm<sup>2</sup>/s using argon units, or a diffusion length of about .4 Å for the 40 ps constant pressure plateaus of the fast runs, or 2 Å for the 1 ns extended plateaus of the runs shown in the inset to Figure 1. A liquid in the laboratory with such a diffusion constant would still be described as a viscous liquid,<sup>6</sup> not a glass; it is basically frozen on time scales of our simulation, though not yet on laboratory time scales.

We have plotted the potential energy as a function of cube root of volume in Figure 4, indicating the point corresponding to  $P_g$  for each temperature. At the beginning of each run, when the pressure is low, thermal fluctuations keep the atoms farther apart on average than would be optimal energetically. As the pressure goes up, atoms move closer together, mapping out a picture of the average potential seen by the ensemble at each density. Clarke<sup>8</sup> noticed such an effect many years ago in simulations of a one-component LJ system, and thought the glass transition would generally tend to occur near the minimum in the potential energy. While this is indeed true at some temperatures, it is not universal. At lower temperatures, diffusion halts before the average spacing even reaches the optimal value, almost as soon as thermal vibrations start forcing atoms into the region dominated

by the repulsive potential, while at higher temperatures, diffusion continues well into the repulsive region.

#### 4. Icosahedral Ordering

It has been previously observed in simulations and experiments in which viscous liquids were cooled into a glassy state that an increase in icosahedral bonding is often associated with vitrification.<sup>2,9</sup> An increase in local icosahedral ordering has also been observed during densification of hard sphere packings.<sup>10</sup> This effect is also seen in the pressure-induced transition, as we now show.

We have analyzed the bonding using a common-neighbor analysis<sup>11</sup> [CNA] in which a set of three indices  $jkl$  specifies the local environment of a bonded pair of atoms. Two atoms are considered bonded if they are within a certain distance of each other, which depends on the type of each. The cutoff is chosen here as the location of the first minimum in the appropriate partial radial distribution function  $g(r)$ . The first index  $j$  is the number of common neighbors, or the number of atoms bonded to both. The next index  $k$  is the total number of bonds between these common neighbors, and  $l$  is the number of bonds in the longest continuous chain formed by the  $k$  bonds between the common neighbors. In an FCC crystal, for example, all bonds would be of the type “421.” Icosahedral bonding results in “555” pairs, as illustrated in Figure 5. Chemical ordering is not reflected in this scheme; the label does not reflect the atomic types of the bonded neighbors.

Because thermal vibrations obscure the underlying order, we use quenched configurations for the structure analysis: a steepest descent minimization of the potential energy under constant pressure is performed until the nearest local minimum on the potential energy surface is reached. We then decompress the quenched configurations, at zero temperature, in order to bring everything to the same state for comparison, as illustrated in Figure 6a. Virtually no structural change is observed upon repeated compression and decompression at zero temperature, as shown in Figure 6b, although this certainly would not be true at any

finite temperature. By bringing everything to the same state for comparison by a route in which activated changes do not occur, we can see the underlying structural changes resulting from activated processes that took place during compression at finite temperatures. The differences we see this way involve energy barriers, and no simple relaxation could take the system from one state to the other.

The nature of the bonding changes as the system rearranges in response to pressure applied at finite temperature. FCC and HCP bonding, identified as 421 and 422 pairs, decrease gradually, and 433 pairs increase gradually, as shown in Figure 7a. The only dramatic change is a strong increase in icosahedral bonding, or 555 pairs, throughout the transition region, stabilizing at a maximum value at about the same pressure as the diffusion constant becomes nearly zero (Figure 7b).

## 5. Isothermal Compressibility

We evaluated the isothermal compressibility,  $\kappa = -\frac{1}{V}(\partial V/\partial p)_T$ , throughout the transition. For all temperatures,  $\kappa$  was a smoothly varying function of pressure, with nothing special at or near  $P_g$ . As indicated in Figure 8 for the  $T^* = 0.8$  run,  $\kappa$  correlates well with the diffusion constant. Both fall together as the pressure increases, although compressibility never goes to zero, but continues to decrease gradually after diffusion is halted. This is because further compression continues to push atoms closer together, further into the repulsive region, but without inducing the structural changes that caused  $\kappa$  to decrease so rapidly with pressure while the material was still liquid. Quenched, decompressed configurations show a 1% increase in density as a result of the structural changes that take place as pressure increases up to the point of structural arrest, so some anomaly in  $\kappa$  would be expected in the transition region. No such anomaly is seen, although a small signal could easily be obscured by the underlying continuous decrease in  $\kappa$  combined with noise in the data.

## 6. WCA radius and Packing Fraction

Hudson and Andersen<sup>12</sup> reported in 1978 that vitrification in binary alloys tends to occur at about the same effective hard-sphere packing fraction, computed using an extension of the method of Weeks, Chandler and Andersen<sup>13</sup> [WCA] for several different materials, and that computer models of hard spheres and LJ fluids performed before that date all gave similar results. The value of this packing fraction,  $\eta_g = \pi\rho R^3/6$ , was  $0.53 \pm 0.02$ . They concluded that the underlying physical process driving the transition is dominated by the repulsive part of the interaction and the simple inability of atoms at this density to slide freely past each other, whatever the details of the interaction potential.

In the years since then many authors have computed the packing fraction at vitrification for various model systems, and have generally concurred with the concept introduced by Hudson and Andersen, although not everyone has obtained the same numbers for the packing fraction, perhaps due partly to differences in the definition of the transition point and in the method for computing the effective radius. For example, Clarke<sup>8</sup> found vitrification in a one-component Lennard-Jones system at a packing fraction of 0.60, but commented in a later paper<sup>6</sup> with Angell and Woodcock that his results were actually consistent with those of Hudson and Andersen if the same criterion for  $T_g$  were applied to both sets of data. Alexanian and Haywood<sup>14</sup> obtained values of .586, .569, and .571 for a hard-sphere system in which the transition point was determined respectively by a signal in the heat capacity, vanishing of the diffusion coefficient, and a calculated equation of state. Berg and coworkers<sup>15</sup> obtained experimental values from fits to viscosity data of .537 for a binary mixture of alkali metals and .547 for a ternary mixture. Pusey and van Megen<sup>16</sup> found that for particles in colloidal suspension, it is .56. Simulations by Cape and Woodcock<sup>17</sup> and by Ullo and Yip<sup>18</sup> gave between .52 and .55 for soft sphere and truncated LJ systems. Abraham<sup>19</sup> found values of .534-.55 for a one-component LJ system using Monte Carlo simulations in which he, like us, studied the effects of squeezing as well as of cooling, and he came to the conclusion that the packing fraction at vitrification is the same for either

squeezing or cooling. Bengtzelius<sup>20</sup> performed theoretical calculations for an LJ fluid and calculated that the effective packing fraction would be .536-.552 at the glass transition, defined as the point at which discontinuities appear in the specific heat and isothermal compressibility.

Following this large and illustrious group, we have also computed an effective WCA packing fraction at vitrification, defined here as the point at which the diffusion coefficient falls below a cutoff of 0.001. We are interested in comparing glasses with different temperature and pressure histories using the same criterion for vitrification and exactly the same method for calculating the hard-sphere radius for each, in order to identify any trends that may exist.

We used the WCA method with the corrections of Verlet and Weiss,<sup>21</sup> as outlined in Appendix B, to compute effective hard-sphere radii  $R$  near vitrification for each of the five temperatures we simulated, as well as for cooling runs at two different pressures,  $P=0$  and  $P=8$ , for comparison.  $R$  is computed analytically based on the number density  $\rho$ , temperature, and the form of the interaction potential. The packing fraction  $\eta$  is then computed as  $\pi\rho R^3/6$ . One subtlety in applying this formalism to a two-component system is that the effective size of the two components does not scale precisely as  $\sigma^3$ ; the large atoms are a bit softer than small atoms, and are thus squeezed more, so they occupy a bit less space. Results reported in this paper are calculated with the approximation that size does scale with  $\sigma^3$ , so that the packing fraction is the same for different species. This assumption is consistent with the work of Lee and Levesque<sup>22</sup> in their analysis of two-component Lennard-Jones systems. Just to be sure, though, we recalculated using the location of the first peak in  $g(r)$  rather than  $\sigma$  to determine relative atomic sizes and thus effective density separately for each component. The final packing fractions  $\eta$  thus obtained agreed to within 2% in every case.

Our results for  $\eta_g$ , the effective packing fraction at the glass transition, are given in Table 1. For the zero-pressure cooling run, we obtain a value  $\eta_g = .564$ , in reasonable agreement with values obtained by others. Glasses prepared at high pressures in the laboratory, accord-



ing to Woodcock, Angell and Cheeseman,<sup>23</sup> tend to have higher densities when examined at normal pressure than the same glasses prepared at normal pressure. Thus, it is not surprising that our values for  $\eta_g$  for the  $P = 8$  cooling run and also for the squeezing runs are higher than those obtained at zero pressure. The reader might be surprised that the packing fraction at  $P_g$  for the  $T^* = 1.5$  run exceeds the hard sphere dense random packing limit of about 0.64, but this limit does not apply here because this is not really a hard sphere system; the WCA radius corresponds closely to the position of the first peak in  $g(r)$ , but some interatomic distances are as much as 12% less than this value, allowing densities that considerably exceed the corresponding hard-sphere limit. What we find remarkable about the results is the trend in  $\eta_g$  for the squeezing runs: the higher the temperature at which the material is compressed, the higher the packing fraction at which diffusion falls below the cutoff.

## 7. DISCUSSION

This trend requires an explanation. It is conceivable that the material is able to densify better when compressed at higher temperature, but we found no evidence for this. Bonding, as determined by a CNA analysis, is the same within error bars for all the structurally arrested final states produced by compression at various temperatures, and also for the  $P = 8$  cooling run. Details of the structure are different in random ways for every run, of course, but the average occurrence of each type of bonded pair is the same within our error bars. Also, when the final states are quenched and then brought to zero pressure, systematic differences in density disappear for the squeezing runs and for the  $P = 8$  cooling run. (We should note that the  $P=0$  cooling runs were different: they produced glassy states that are intrinsically less dense, and with slightly different bonding.) The large systematic increase in  $\eta_g$  with higher temperature for compression is thus not associated with any intrinsic structural differences that we could detect in the glassy states produced.

There is a more subtle structural difference however: as the material densifies during

squeezing, the first part of the split second peak of  $g(r)$  increases in height, and when  $g(r)$  is scaled by the location of the first peak, the second and further peaks move closer, as illustrated in Figure 9. We have found a small, but consistent, trend in  $g(r)$  scaled by the location of the first peak at the glass transition: for higher temperature compression runs, the second, third and fourth peaks are located at smaller values of  $r$ . These values continue to decrease somewhat past the pressure at which diffusion falls below the cutoff, and then stabilize.

A structural measure of the transition point, then, could be defined as the pressure  $P_g$  for which further compression results in no change in the scaled  $g(r)$  function because no further structural changes can occur. Another manifestation of structural arrest is that the volume after quenching and then releasing the pressure becomes constant. (Quenching eliminates the temperature-dependent thermal expansion, and releasing the pressure eliminates the overall rescaling of atomic positions, allowing direct comparison of states with different histories.) This is plotted for our  $T^* = 0.8$  run in Figure 10. Another correlated property is the disappearance of anharmonicity: the only change the structurally arrested state undergoes when quenched is the elimination of thermal noise, or gaussian fluctuations of the atoms about their average positions. The rms value  $(\langle x - x_0 \rangle^2)^{1/2}$  of these fluctuations is proportional to temperature, so when the harmonic system is quenched and atomic locations before and after the quench are compared, the average rms difference is proportional to temperature, and independent of pressure history or anything else. This is certainly not the case for the liquid state, in which quenching induces considerable non-activated structural changes. Rms differences for the quenched versus unquenched configuration of the viscous fluid decrease with pressure until structural arrest is reached, at which point they settle down to a constant, as shown in Figure 10.

We have measured these three properties for the  $T^* = 0.8$  run, and have found that all three give results consistent with the conclusion of structural arrest occurring at a pressure of 14. This is higher than the pressure of 10.5 at which diffusion falls below the cutoff of 0.001; diffusion essentially ceased before pressure stopped having any effect on the structure

of the system.

The preceding three methods are unsuitable for detailed analysis of all the data. Changes in  $g(r)$  are small, so the uncertainty in locating the point at which  $g(r)$  stops changing is large. The other two methods involve quenches, which are expensive. A more usable method, introduced by Ullo and Yip,<sup>18,24</sup> determines structural arrest from pressure versus density plots. At high pressures, the density of the glass is essentially linear in pressure, or vice versa for those who simulate by imposing a density and measuring the pressure, as shown in Figure 11. Ullo and Yip define the density of the transition point as the intersection of a straight line through the high-density points with a line drawn through the lowest density points. Even a generous reader would disapprove if we tried to draw a straight line through our non-linear low density data, so we will use a slightly different definition:  $\rho_g$  is the density at which  $\rho$  begins to deviate from the linear behavior of the high-density data. For the  $T^* = 0.8$  data, the point at which structural arrest was determined to occur by other methods is at  $P = 14$ , and the density at this point deviates from the value predicted by the linear behavior of the higher density points by 1.4%. We therefore define the structural transition pressure  $P_g^s$  for the squeezing runs by the criterion that it is the lowest pressure at which density is within 1.5% of the value extrapolated from the high density linear region.

The values thus obtained for  $P_g^s$ , with the corresponding packing fractions  $\eta_g^s$ , are shown in Table 2. There is a small systematic decrease in  $\eta_g^s$  with increasing temperature, which is reasonable since temperature effects are included in the WCA calculation. The structural similarity between all the final states, at  $P > P_g^s$ , as measured by a CNA analysis of local bonding and by the density after quenching and decompressing, implies that they are all similar at the point of structural arrest.<sup>25</sup> Once a maximally dense type of configuration is attained, barriers to further structural relaxation in response to pressure apparently diverge rapidly: we do not observe any tendency for the higher temperature runs to achieve denser final states than those squeezed at lower temperature.

If the structure is similar at the point of structural arrest, then the distribution of barriers to diffusion at this point must be similar. We have determined this effective energy barrier

by plotting the diffusion coefficient at the point of structural arrest,  $D_g^s$ , against the inverse temperature, as shown in Figure 12. This clearly shows thermally activated behavior with a high activation energy,  $4.4\epsilon$ , associated with diffusion near the point of structural arrest. The material at this point is densely packed, each atom is in a cage formed by 12 or so tightly pressed neighbors, and atomic rearrangement requires crossing a barrier corresponding to the strength of 4.4 interatomic bonds.

We thus see that a definition of the glass transition as the point at which further increases in pressure induce no structural changes is qualitatively different from a definition measuring the point at which diffusion reaches some constant cutoff, although it is equivalent to a definition involving diffusion if a thermally activated cutoff is used. This distinction exists only for the glass transition caused by increasing pressure: in the transition caused by cooling, there is no changing pressure or any other driving force to induce structural change, so all structural rearrangement stops when diffusion stops. The difference between the two definitions may not be significant in the laboratory, since the glass transition is sharp under long time scales, but in computer simulations, in which the transition is smeared out almost beyond recognition (some readers might prefer to leave out the “almost”), it is important to distinguish between the two.

The increase with temperature of our effective packing fraction  $\eta_g$  is now understood: the transition point defined by a constant cutoff in the diffusion coefficient, although it is a natural extension of the customary laboratory definition, is not well correlated with structural properties, and  $\eta_g$  is a structural property. At higher temperatures, diffusion continues at a level above the cutoff until the material is closer to the final glassy configuration than at lower temperatures, thus achieving a higher value for  $\eta_g$ .

## 8. Conclusions

Of the structural changes that occur as a two-component LJ system is compressed at constant temperature, the most noticeable is a two-fold increase in icosahedral ordering, as in

the transition caused by cooling at constant pressure. The glass has essentially the same structure whether it was produced by squeezing at low or high temperature or by cooling under pressure: atoms are bonded in the same way, and the volume after quenching and then releasing the pressure is the same. Subtle differences presumably do exist, but their effect on at least these two structural probes is small.

The effective hard-sphere packing fraction computed using the WCA method at the pressure  $P_g$  for which diffusion falls below a given cutoff was found to depend on the temperature at which the material was compressed: it was higher for high temperature runs. This resulted, not from any fundamental difference caused by squeezing at higher temperature, but rather from the fact that pressure-driven structural effects are not well correlated with the diffusion coefficient at any constant time scale. Pressure-induced structural changes, which for low temperatures continue to occur well beyond the density at which diffusion becomes immeasurably small, result in a denser final structure for the compressed glass than is achieved by cooling at zero pressure, with a correspondingly higher effective packing fraction.

The glass transition point defined in terms of a constant cutoff in diffusion, analagous to a constant cutoff in viscosity, is not equivalent to the transition point defined in terms of structural properties. Because diffusion is a thermally activated process, the better correlated definition involves an exponential, thermally activated form for the cutoff in diffusion. The activation energy thus found to be associated with diffusion at the point of structural arrest is large: we estimate it to be about  $4.4 \epsilon$ .

## 9. Appendix A: Choosing the Piston Mass

Andersen’s method<sup>3</sup> for running isobaric M. D. simulations couples an extra degree of freedom, the volume of the system, into the equations of motion. To do this, an effective “piston mass” is needed, which sets the relative strength of the volume term. Equilibrium properties of the system are not actually affected by the piston mass, but dynamical properties are, and using an inappropriate value can slow the approach to equilibrium. According to Andersen,<sup>3</sup> the correct piston mass to use is such that the time scale for fluctuation of the volume of the sample is equivalent to the time scale for sound waves to travel through the sample.

We show how to do this here, deriving a simple formula that can be applied frequently during the simulation to rescale the piston mass  $M_p$  appropriately.

The pressure and volume of the system are functions of the atomic coordinates. However, by including an overall scaling factor for the coordinates, volume can be treated as an independent variable.

The equation of motion for the volume is:

$$M_p \ddot{V} = P - P_{eq} \quad (1)$$

where  $P_{eq}$  is the externally applied, equilibrium pressure. (So if  $P > P_{eq}$ , a force acts to raise the overall scaling factor and thus the volume, which reduces the pressure.) We can Taylor expand  $V$  as follows:

$$\begin{aligned} V &= V_{eq} + (P - P_{eq}) \frac{dV}{dP}|_{eq} + \dots \\ &= V_{eq} - (P - P_{eq}) \kappa V_{eq} + \dots \end{aligned} \quad (2)$$

where  $\kappa$  is the isothermal compressibility  $\kappa_T$  for simulations in an isothermal ensemble (as in this paper), or the adiabatic compressibility  $\kappa_s$  for simulations in a microcanonical ensemble:

$$\kappa = -\frac{1}{V_{eq}} \frac{\partial V_{eq}}{\partial P}|_{s \text{ or } T}. \quad (3)$$

Ignoring higher order terms, this gives a differential equation for  $V$ :

$$M_p \ddot{V} = -(V - V_{eq})/(\kappa V_{eq}) = -M_p \omega^2 (V - V_{eq}) \quad (4)$$

where

$$\omega \equiv (M_p \kappa V_{eq})^{-1/2}. \quad (5)$$

We want to choose  $M_p$  so that the period  $T = 2\pi/\omega$  corresponds to the time it takes a sound wave, velocity  $v_s$ , to travel the length of the box,  $V_{eq}^{1/3}$  :

$$2\pi/\omega = V_{eq}^{1/3}/v_s \implies M_p = [(2\pi v_s)^2 \kappa V_{eq}^{1/3}]^{-1}. \quad (6)$$

We now note that  $v_s$  is related<sup>26</sup> to the adiabatic compressibility  $\kappa_s$  :

$$v_s^2 = 1/(\kappa_s \rho) \quad (7)$$

where  $\rho$  is the mass density, so for adiabatic simulations,

$$M_p = \frac{\rho}{4\pi^2 V_{eq}^{1/3}}. \quad (8)$$

For isothermal simulations, we need to substitute  $\kappa_T = \gamma \kappa_s$ , where  $\gamma = c_p/c_v$ , the ratio of the specific heats. We have approximated this ratio  $\gamma$  as unity in the current work, simply using the same expression for  $M_p$  as would be appropriate for adiabatic simulations. This admittedly introduces a systematic underestimation of  $M_p$  by several percent; should a more accurate value for  $M_p$  be required, a more accurate estimate of  $\gamma$  should be used.

## 10. Appendix B: Effective hard-sphere radius

We give here a brief sketch of how we computed the effective hard-sphere radius using the WCA method<sup>13</sup> with the corrections of Verlet and Weiss<sup>21</sup>. All of this is published elsewhere, but we have attempted to sketch the entire procedure here in one place in a way that enables the reader to quickly set up a similar calculation using, for example, a mathematical symbolic manipulation program.

The goal is to find the radius of the hard-sphere system that most closely resembles a system of particles interacting through some other kind of potential, in our case, the Lennard-Jones potential.

The WCA method is appropriate for potentials which have a strong repulsive core. With this assumption, the approximation is made that the function  $y(r) = g(r)e^{\beta v_0(r)}$  is similar to that of a hard-sphere system, so the radial distribution function  $g(r)$  may be written as  $g(r) \approx e^{-\beta v_0(r)} y_{HS}(r)$ , where  $v_0(r)$  is the repulsive part of the potential. For the Lennard-Jones system,

$$v_0(r) = \begin{cases} 4\epsilon[(\sigma/r)^{12} - (\sigma/r)^6] + \epsilon & r < 2^{1/6}\sigma \\ 0 & r \geq 2^{1/6}\sigma. \end{cases} \quad (9)$$

Taking the Fourier transform of  $g(r)$  to get the structure factor and equating the structure factor for the model system to that of a hard-sphere system at  $\vec{k} = 0$  gives<sup>27</sup> the WCA formula for the effective hard-sphere radius of a system with repulsive potential  $v_0(r)$  :

$$\int_0^\infty y_{HS} \times (1 - e^{-\beta v_{HS}(r)}) r^2 dr = \int_0^\infty y_{HS} \times (1 - e^{-\beta v_0(r)}) r^2 dr \quad (10)$$

where

$$v_{HS}(r) = \begin{cases} \infty & r \leq R \\ 0 & r > R. \end{cases} \quad (11)$$

It might seem that just setting the  $\vec{k} = 0$  peaks equal would be inadequate, that the structure factor should really be matched as closely as possible over its entire range, for example by minimizing the integral over the whole range, but Verlet and Weiss have performed both calculations and found effective hard-sphere radii that agree to within a few tenths of a percent<sup>28</sup> so we will use the simpler WCA criterion here.

To get the function  $y_{HS}$  needed for calculating  $R$ , we begin with the expression given by Wertheim,<sup>29</sup> in the form given by Throop and Bearman<sup>30</sup> (with typographical errors corrected), for the radial distribution function  $g(r)$  for hard spheres in the Percus-Yevick approximation. For hard spheres,  $g(r) = 0$  for  $r < R$ . Since  $R$  always comes out pretty close



to  $\sigma$ , certainly always within a factor of 2, we only need the part for  $R < r < 2R$  here, which is:

$$g_w(x, \eta) = \frac{1}{(12\eta x)} \sum_1^3 \lim_{t \rightarrow t_i} [(t - t_i) \frac{tL(t)e^{t(x-1)}}{S(t)}] \quad (12)$$

$$L(t) = 12\eta[(1 + \eta/2)t + (1 + 2\eta)]$$

$$S(t) = (1 - \eta)^2 t^3 + 6\eta(1 - \eta)t^2 + 18\eta^2 t - 12\eta(1 + 2\eta)$$

$$x = r/R$$

$$\eta = \frac{\pi}{6} \rho R^3, \quad (13)$$

where  $\rho$  is the number density. The sum is over the three roots of  $S(t)$ .

This  $g(r)$  can be more conveniently written as:

$$g_w(x, \eta) = \frac{1}{12\eta x(1 - \eta)^2} \left[ \frac{z_1 e^{z_1(x-1)} L(z_1)}{(z_1 - z_2)(z_1 - z_3)} + \frac{z_2 e^{z_2(x-1)} L(z_2)}{(z_2 - z_1)(z_2 - z_3)} + \frac{z_3 e^{z_3(x-1)} L(z_3)}{(z_3 - z_1)(z_3 - z_2)} \right] \quad (14)$$

where  $\{z_1, z_2, z_3\}$  are the three roots of  $S(t)$ .

What we need is  $y(r) = g(r) - c(r)$ . The direct correlation function  $c(r)$  is zero for  $r > R$ , and Wertheim gives the following approximation for  $r < R$ :

$$c_w(r) = \begin{cases} -[(1 + 2\eta)^2 - 6\eta(1 + \eta/2)^2 x + \eta/2(1 + 2\eta)^2 x^3]/(1 - \eta)^4 & r < R \\ 0 & r \geq R. \end{cases} \quad (15)$$

Verlet and Weiss point out that this  $y(r)$  does not match simulation results for hard spheres well, but that it can be substantially improved by a rescaling and the addition of an extra function. Their improved  $y(r)$  is

$$y_{vw}(r/R, \eta) = g_w(x', \eta') - c_w(x', \eta') + \delta g_1(r, R, \eta), \quad (16)$$

with the rescaled variables

$$\eta' = \eta(1 - \eta/16)$$

$$x' = x(1 - \eta/16)^{-1/3}. \quad (17)$$

The extra function  $\delta g_1(r, R, \eta)$  is apparently added over the entire range  $0 < r < 2R$ .

$$\delta g_1(r, R, \eta) = \frac{A}{r} e^{-\mu(r-R)} \cos[\mu(r-R)] \quad (18)$$

$$A \approx \frac{3}{4} R \frac{\eta'^2 (1 - 0.7117\eta' - 0.114\eta')^2}{(1 - \eta')^4} \quad (19)$$

$$\mu \approx \frac{24A/R^2}{\eta' g_w(1, \eta')}. \quad (20)$$

More accurate, though more complicated, formulas for  $A$  and  $\mu$  and also for  $c(r)$  have been given by Henderson and Grundke,<sup>32</sup> but we use the simpler Verlet approximations here.

The effective hard-sphere radius, finally, is  $R$  for which equation 2, which may be rewritten this way, is satisfied:

$$\begin{aligned} \int_0^R (-c_w(x', \eta') + \delta g_1(r, R, \eta)) r^2 dr &= \int_0^R (-c_w(x', \eta') + \delta g_1(r, R, \eta)) (1 - e^{-\beta v_0(r, \sigma)}) r^2 dr \\ &+ \int_R^{2^{1/6}\sigma} g_w(x', \eta') + \delta g_1(r, R, \eta)) (1 - e^{-\beta v_0(r, \sigma)}) r^2 dr \quad (21) \end{aligned}$$

We note in passing that while the form for  $c(r)$  used here is, according to Henderson and Grundke,<sup>32</sup> quite poor, the final answer for  $R$  is quite insensitive to it. In fact, we originally computed  $R$  with  $\delta g_1(r, R, \eta)$  added only for  $r > R$ , and the results for  $R$  differed from the current results by only a few tenths of a percent.

## ACKNOWLEDGMENTS

This research was sponsored by the NSF under grant CHE-9217774. S.L.S. thanks Arthur P. Smith for many helpful discussions.

\* Present Address: Department of Chemistry, University of British Columbia, Vancouver, BC, Canada V6T1Y6

## REFERENCES

1. A few of the most recent papers include: K. F. Ould and G. Pastore, Mol. Phys. **81**, 1011 (1994); T. Tomida and T. Egami, Phys. Rev. B **48**, 3048 (1993); D. Thirumalai and R. D. Mountain, Phys. Rev. E **47**, 479 (1993); S. Ranganathan and G. S. Dubey, J. Phys. Cond. Matt. **5**, 387 (1993); C. Dasgupta and S. Ramaswamy, Physica A **186**, 314 (1992).
2. H. Jónsson and H. C. Andersen, Phys. Rev. Lett. **60**, 2295 (1988).
3. H. C. Andersen, J. Chem. Phys. **72**, 2384 (1980).
4. J. R. Fox and H. C. Andersen, J. Phys. Chem. **88**, 4019 (1984).
5. The behavior of  $D_\alpha$  is the same for both species, although about 30-40% higher for the smaller atoms; we could have used  $D_1$  instead of  $D$ , or have averaged in a different way, without changing any of the conclusions in this paper.
6. C. A. Angell, J. H. R. Clarke and L. V. Woodcock, Advan. Chem. Phys. **48** 397 (1981).
7. P. W. Anderson, in *Ill-Condensed Matter*, ed. by R. Balien, R. Maynard and G. Toulouse (North-Holland, 1979).
8. J. H. R. Clarke, J. Chem. Soc. Far. Trans. 2 **75**, 1371 (1979).
9. See, for example: V. A. Likhachev, A. I. Mikhailin, and L. V. Zhigilei, Phil. Mag. A, **69**, 421 (1994); L. Cervinka, J. Non-Cryst. Sol. **156**, 94 (1993); R. S. Liu, D. W. Qi and S. Wang, Phys. Rev. B **45**, 451 (1992); D. W. Qi and S. Wang, Phys. Rev. B **44**, 884 (1991); T. Kondo, K. Tsumuraya and M. S. Watanabe, J. Chem. Phys. **93**, 5182 (1990).
10. A. S. Clarke and H. Jónsson, Phys. Rev. E **47**, 3975 (1993).
11. D. Faken and H. Jónsson, Comp. Mat. Sci. **2**, 279 (1994).
12. S. Hudson and H. C. Andersen, J. Chem. Phys. **69**, 2323 (1978).

13. J. D. Weeks, D. Chandler and H. C. Andersen, J. Chem. Phys. **54**, 5237 (1971).
14. M. Alexanian and T. W. Haywood, Physica A **157**, 797 (1989).
15. R. F. Berg, M. R. Moldover, S. Rabinovich and A. Voronel, J. Phys. F: Met. Phys. **17** 1861 (1987).
16. P. N. Pusey and W. van Megan, Phys. Rev. Lett. **59** 2083 (1987).
17. J. N. Cape and L. V. Woodcock, J. Chem. Phys. **72**, 976 (1980).
18. J. Ullo and S. Yip, Phys. Rev. A **39**, 5877 (1989).
19. F. F. Abraham, J. Chem. Phys. **72**, 359 (1980).
20. U. Bengtzelius, Phys. Rev. A **33**, 3433 (1986). A summary of other peoples' values for  $\eta_g$  is included in this paper.
21. L. Verlet and J.-J. Weis, Phys. Rev. A **5**, 939 (1972).
22. L. L. Lee and D. Levesque, Mol. Phys. **26**, 1351 (1973).
23. L. V. Woodcock, C. A. Angell and P. Cheeseman, J. Chem. Phys. **65**, 1565 (1976).
24. J. J. Ullo and S. Yip, Phys. Rev. Lett. **54**, 1509 (1985).
25. This is certainly true for the three lower temperature runs, for which diffusion is minimal beyond the point of structural arrest. Some changes could occur beyond  $P_g^s$  for the  $T = 1.5$  run since diffusion continues, but if these involved significant structural changes, the final configuration should be intrinsically denser than for the lower temperature runs, which it is not.
26. See, for example, L. Tisza, *Generalized Thermodynamics* (The M.I.T. Press, 1966), p. 74-75.
27. See pages 5239-5240 of reference 13 for details.

- 28. Table III of reference 21.
- 29. M. S. Wertheim, Phys. Rev. Lett. **10**, 321 (1963).
- 30. G. J. Throop and R. J. Bearman, J. Chem. Phys. **42**, 2408 (1965).
- 31. L. V. Woodcock, Ann. N.Y. Acad. Sci. **371** (*Structure and Mobility in Molecular and Atomic Glasses*), 274 (1981).
- 32. D. Henderson and E. W. Grundke, J. Chem. Phys. **63**, 601 (1975).

## FIGURES

Fig. 1. For each temperature simulated, pressure increases over time in a stepwise fashion, with brief periods of constant, though fluctuating, pressure alternating with linearly increasing applied pressure. For one temperature,  $T^* = 0.8$ , we also ran long constant pressure runs from the endpoint configurations of the short plateaus as illustrated in the inset. Results from both are included in data plotted in other figures.

Fig. 2. Average diffusion constant  $D$ , in units of  $\sigma_{11}^2/\tau$ , with fitting functions as described in the text. The three different symbols for  $T^* = 0.8$  correspond respectively to the regular short-plateau run of Figure 1, the extended-plateau run of the inset to Figure 1, and a third run in which the average rate of pressure increase was slower by about a factor of 8 than in the short-plateau run.

Fig. 3. The transition pressure  $P_g$  in the main figure is defined as the pressure at which the diffusion constant falls below a cutoff of 0.001. The inset shows similar curves for cutoffs ranging from 0.0005 to 0.004.

Fig. 4. Average effective potential as a function of average interatomic spacing, with the point corresponding to  $P_g$  from Figure 3 indicated for each temperature.

Fig. 5. The dark atoms illustrated here form a 555 bonded pair: they have 5 common neighbors, there are 5 bonds between the common neighbors, and the longest chain of bonds between the common neighbors consists of 5 bonds. An icosahedron is formed of 12 pairs bonded in this way; one of the dark atoms and each of the light atoms here, paired with the other dark atom, is one of the 12 pairs, so the atoms shown here comprise the central atom and half the outer atoms of a complete icosahedron. We therefore refer to 555 pairs as “icosahedrally bonded.”

Fig. 6. a. Each run produces configurations at a sequence of increasing pressures at a given temperature. In order to compare the underlying differences between them, we bring them all into the same state by quenching to zero temperature, then releasing the pressure.

b. We took a quenched state and alternately applied and released a pressure of  $13 (\epsilon/\sigma^3)$ . Almost no structural change was observed. The number of 555 pairs is computed based on a cutoff in the maximum distance between bonded pairs. We scaled the cutoff by the length scale  $V^{1/3}$  in order to compare configurations in different pressure states. Because the distribution of bond lengths changes slightly under pressure, this resulted in a slight difference in the number of pairs found in the compressed states relative to the uncompressed states, even though no rearrangements actually occurred. This illustrates the subtlety involved in trying to compare configurations at different pressures, which is why we generally bring configurations into the same zero-temperature zero-pressure state before making comparisons.

Fig. 7. a. Bonding. We show here the number of pairs of several types throughout the glass transition. The top curve, showing “555” (icosahedrally bonded) pairs, is the same as in Figure 7b. The occurrence of “421” and “422” pairs, associated with FCC and HCP bonding, and also “433” pairs, decreases gradually throughout the transition, while “544” pairs, associated with distorted icosahedra, increase slightly.

b. Diffusion and Icosahedral Bonding. The top curve shows the number of icosahedrally bonded pairs increasing throughout the glass transition for a run at  $T^* = 0.8$ . Each point is an average over the number of 555 pairs in five different configurations that had been raised to and held at a pressure  $P$ ; each configuration was quenched and decompressed before the structural computation. The bottom curves show the diffusion constant,  $D_A$  for small atoms and  $D_B$  for large ones, decreasing through the same transition.



Fig. 8. Diffusion and Isothermal Compressibility. The compressibility  $\kappa$  decreases rapidly in the region where structural changes are occurring to accommodate the increasing pressure, and then only gradually after vitrification, where pressure continues to force atoms closer together, but without inducing structural relaxation. As in Figure 8,  $D_A$  and  $D_B$  are diffusion constants for small and large atoms respectively.

Fig. 9. Radial distribution function for component 1 at and beyond  $P_g$ . The lower two curves show the rdf, scaled by the WCA radius, at the transition point as defined by a constant diffusivity cutoff for systems compressed at  $T^* = 0.6$  and at  $T^* = 1.5$ . The upper curve is the scaled rdf for the  $T^* = 0.6$  run at a much higher pressure. Only this latter curve depicts a fully densified structure: in the lower curves, the split second peak is not yet fully developed and the more distant peaks have not stopped moving in relative to the first peak. The structurally arrested material of the upper curve undergoes no further changes except for an overall scaling factor with further increases in pressure, while the material at the diffusivity-determined  $P_g$  has not yet reached this point. Of the two lower curves, the  $T^* = 1.5$  one is more like the upper curve; the second and further peaks are slightly closer together because the material has proceeded farther toward structural arrest by the time diffusion stops than has the  $T^* = 0.6$  material.

Fig. 10. Probes of structural arrest. The upper curve shows the rms difference between atomic positions before and after quenching as a function of pressure; the harmonic limit is reached at a pressure of 14. The lower curve shows the volume after quenching and releasing the pressure; this stops decreasing at a pressure of 14, indicating that the material is fully densified and structurally arrested, so that further increases in pressure induce no further structural changes.

Fig. 11. Density versus Pressure. This data is for  $T^* = 1.5$ . The dark point, which is identified as the structural transition point, is where the deviation from the approximately linear behavior of higher pressures reaches 1.5%.

Fig. 12. Diffusion Coefficient at the Structural Transition Point. The natural logarithm of the diffusion coefficient at the pressure  $D_g^s$  at which structural arrest occurs, determined as shown in Figure 11, is well described by a thermally activated form with an activation energy of  $4.4 \epsilon$ . Temperature, as usual, is in units of  $\epsilon/k_B$ .

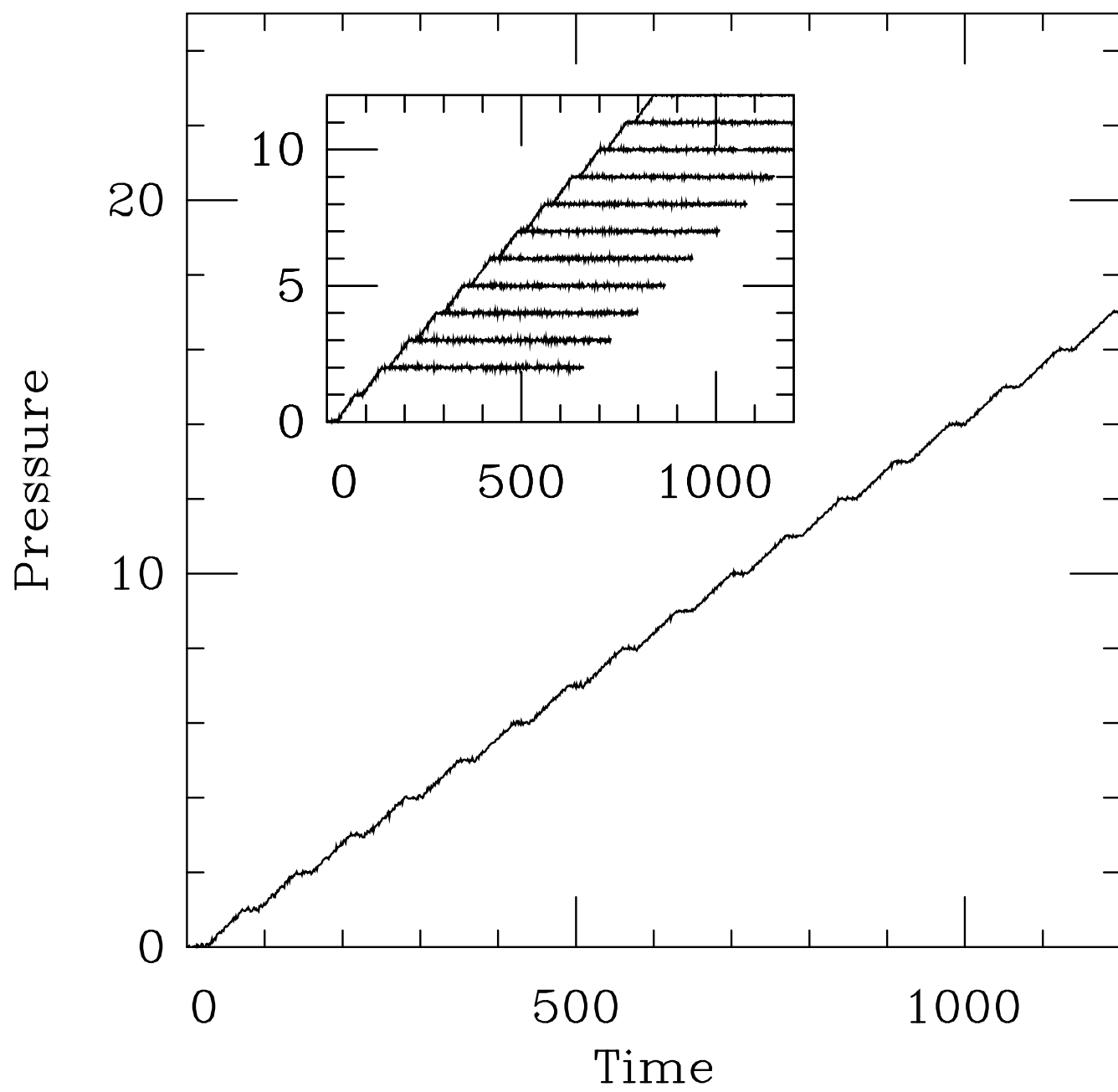
# TABLES

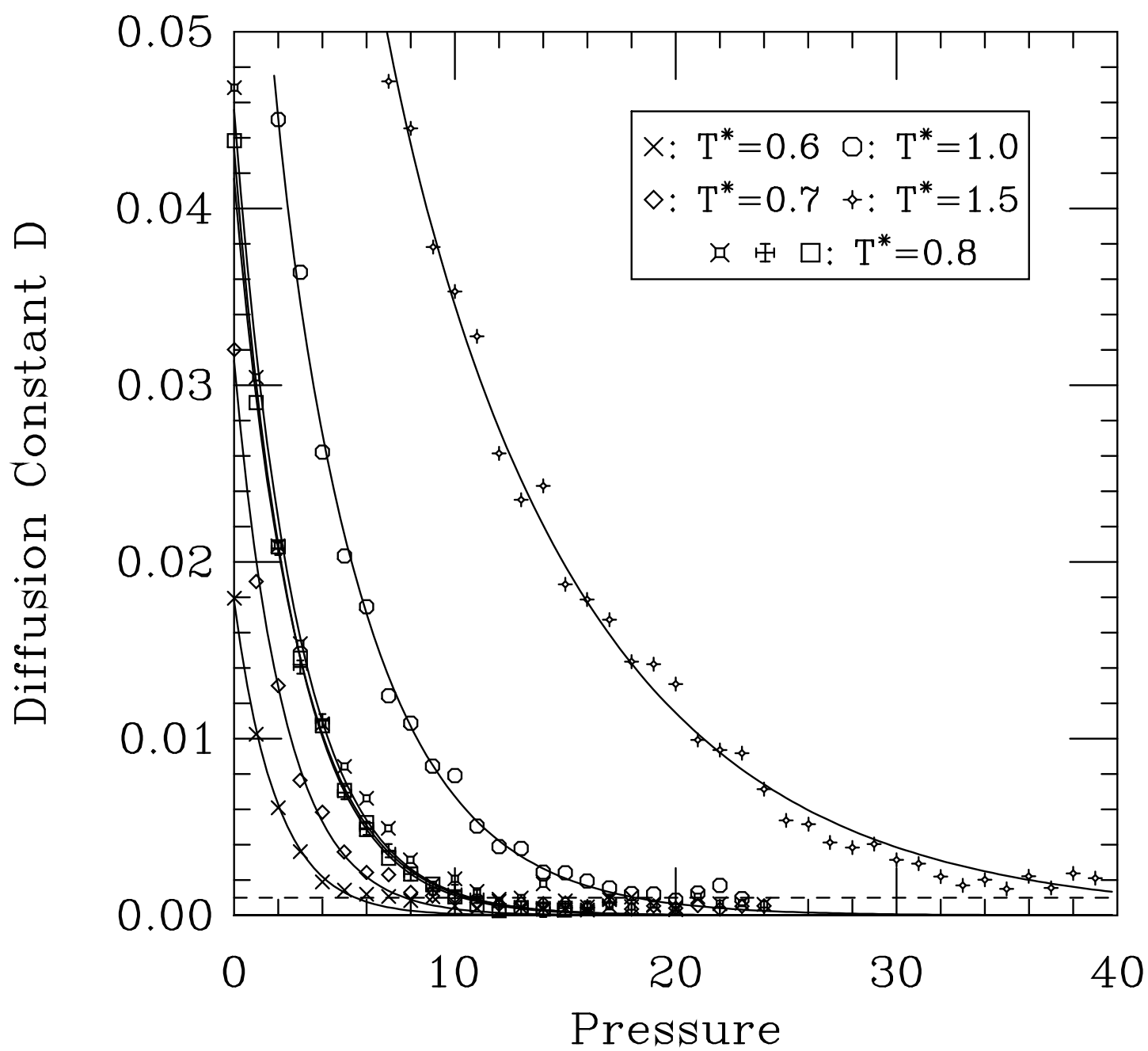
Table 1. Effective packing fraction  $\eta_g$  near the point  $P_g$  at which diffusion falls below the cutoff. Values near the analogous point  $T_g$  for two cooling runs are also given for comparison. Calculation of  $\eta_g = (\pi/6) \rho R_{WCA}^3$  requires calculation of an effective radius  $R_{WCA}$  for the particles, which is a function of temperature and density.

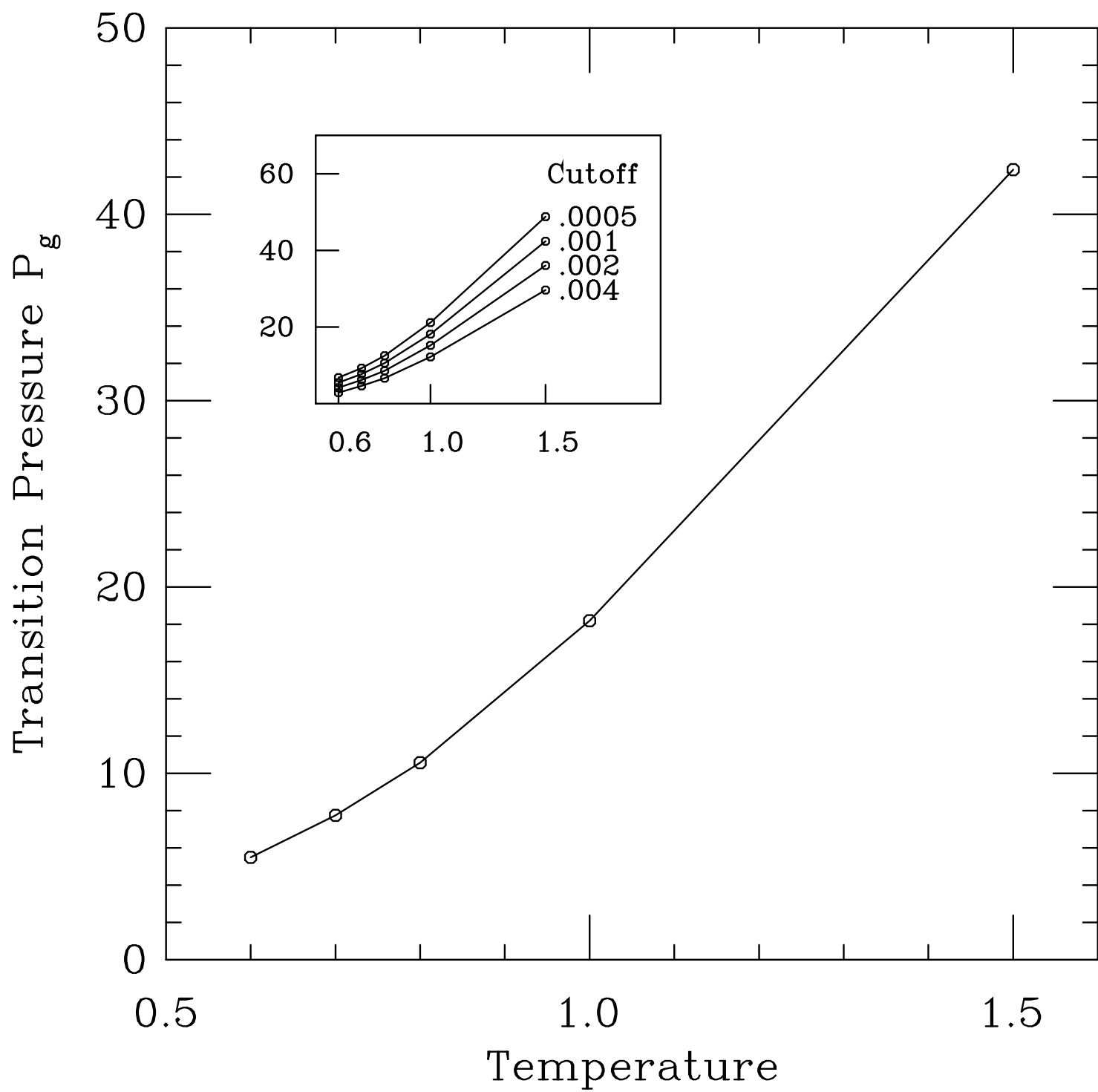
Point	Temperature	Pressure	Density	$R_{WCA}$	$\eta_g$
$P_g$	0.6	5.49	0.908	1.0270	0.590
$P_g$	0.7	7.74	0.929	1.0213	0.594
$P_g$	0.8	10.47	0.952	1.0161	0.599
$P_g$	1.0	18.18	1.007	1.0070	0.617
$P_g$	1.5	42.40	1.121	0.9913	0.655
$T_g$	0.35	0	0.829	1.0430	0.564
$T_g$	0.65	8	0.936	1.0228	0.601

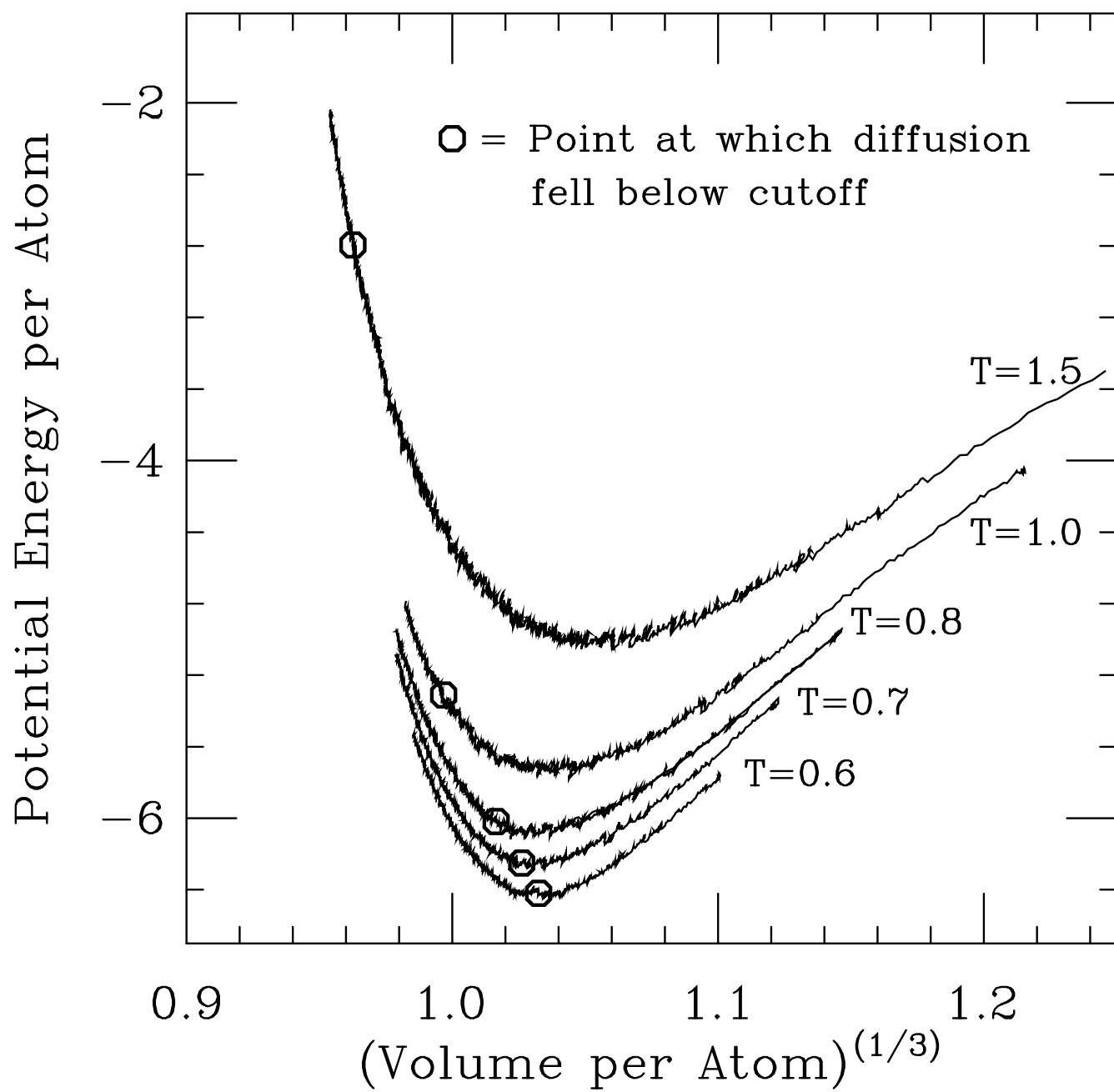
Table 2. Effective packing fraction  $\eta_g^s$  near the point of structural arrest,  $P_g^s$ . The systematic trend in the packing fraction  $\eta_g^s$  reflects temperature effects included in the WCA calculation; other measures indicate that the structure at the point of structural arrest is similar for all the runs, as discussed in the text.

Temperature	Pressure	Density	$R_{WCA}$	$\eta_g^s$
0.6	10	0.965	1.0259	0.625
0.7	11	0.968	1.0206	0.617
0.8	14	0.988	1.0155	0.620
1.0	15	0.979	1.0074	0.600
1.5	25	1.021	0.9908	0.596









A 555 pair

